

The entire code repository used to calculate the data for this report, and the **tex** file used to produce this **pdf** document, can be found at <https://github.com/dgsaf/acqm-workshop-2>.

Theory

Basis

We utilise a complete basis of the form, $\mathcal{B} = \{|\phi_i\rangle\}_{i=1}^N$, where the basis functions are represented in coordinate-space in the form

$$\phi_i(r, \Omega) = \frac{1}{r} \varphi_{k_i, \ell_i}(r) Y_{\ell_i}^{m_i}(\Omega) \quad \text{for } i = 1, \dots, N \quad (1)$$

where the radial functions, $\mathcal{R} = \{|\varphi_{k_i, \ell_i}\rangle\}_{i=1}^N$ form a complete basis for the radial function space, in the limit as $N \rightarrow \infty$. We utilise a Laguerre basis for the set of radial functions which, for $k = 1, 2, \dots$ and where $\ell \in \{0, 1, \dots\}$, are of the following form in coordinate-space

$$\varphi_{k, \ell}(r) = N_{k, \ell} (2\alpha_\ell r)^{\ell+1} \exp(-\alpha_\ell r) L_{k-1}^{2\ell+1}(2\alpha_\ell r) \quad (2)$$

where $\alpha_\ell \in (0, \infty)$ are arbitrarily chosen constants, where $N_{k, \ell}$ are the normalisation constants, given by

$$N_{k, \ell} = \sqrt{\frac{\alpha_\ell (k-1)!}{(k+\ell)(k+2\ell)!}} \quad (3)$$

and where $L_{k-1}^{2\ell+1}$ are the generalised Laguerre polynomials.

Overlap Matrix Elements

The overlap matrix elements, $B_{i,j}$, are of the form

$$B_{i,j} = \langle \phi_i | \phi_j \rangle = \langle \frac{1}{r} \varphi_{k_i, \ell_i} | \frac{1}{r} \varphi_{k_j, \ell_j} \rangle \langle Y_{\ell_i}^{m_i} | Y_{\ell_j}^{m_j} \rangle = \langle \frac{1}{r} \varphi_{k_i, \ell_i} | \frac{1}{r} \varphi_{k_j, \ell_j} \rangle \delta_{\ell_i, \ell_j} \delta_{m_i, m_j} \quad (4)$$

where

$$\langle \frac{1}{r} \varphi_{k_i, \ell_i} | \frac{1}{r} \varphi_{k_j, \ell_j} \rangle = \begin{cases} 1, & \text{if } k_i = k_j \\ -\frac{1}{2} \sqrt{1 - \frac{\ell(\ell+1)}{(k_i + \ell)(k_i + \ell + 1)}}, & \text{if } k_j = k_i + 1 \\ \langle \frac{1}{r} \varphi_{k_j, \ell_j} | \frac{1}{r} \varphi_{k_i, \ell_i} \rangle, & \text{if } k_i = k_j + 1 \\ 0, & \text{otherwise} \end{cases} \quad (5)$$

Kinetic Matrix Elements

The kinetic matrix elements, $K_{i,j}$, are of the form

$$K_{i,j} = \langle \phi_i | \hat{K} | \phi_j \rangle = \alpha^2 (\delta_{k_i, k_j} - \frac{1}{2} \langle \frac{1}{r} \varphi_{k_i, \ell_i} | \frac{1}{r} \varphi_{k_j, \ell_j} \rangle) \delta_{\ell_i, \ell_j} \delta_{m_i, m_j} \quad (6)$$

Spherically-Symmetric Potential Matrix Elements

For a spherically symmetric potential, $V(r, \Omega) = V(r)$, the potential matrix elements can be calculated numerically to be of the form

$$V_{i,j} = \langle \phi_i | \hat{V} | \phi_j \rangle = \langle \frac{1}{r} \varphi_{k_i, \ell_i} | \hat{V} | \frac{1}{r} \varphi_{k_j, \ell_j} \rangle \delta_{l_i, l_j} \delta_{m_i, m_j} \quad (7)$$

where

$$\langle \frac{1}{r} \varphi_{k_i, \ell_i} | \hat{V} | \frac{1}{r} \varphi_{k_j, \ell_j} \rangle = \int_0^\infty dr \varphi_{k_i, \ell_i}(r) V(r) \varphi_{k_j, \ell_j}(r). \quad (8)$$

1 H_2^+ Potential-Energy Curves

Details of Relevant Theory and Code

Axially-Symmetric Potential

The axially-symmetric potential of the H_2^+ molecule, with two nuclei at $\mathbf{R} = (0, 0, \pm \frac{R}{2})$, can be written in the form

$$V(r, \Omega) = - \left(\frac{1}{\|\mathbf{r} + \mathbf{R}\|} + \frac{1}{\|\mathbf{r} - \mathbf{R}\|} \right) \quad (9)$$

which can be written alternatively, using the multipole expansion, in the form

$$V(r, \Omega) = -2 \sum_{\lambda \in E} \sqrt{\frac{4\pi}{2\lambda+1}} \frac{r_{<}^\lambda}{r_{>}^{\lambda+1}} Y_\lambda^0(\Omega) \quad (10)$$

where $r_{<} = \min(r, \frac{R}{2})$, $r_{>} = \max(r, \frac{R}{2})$, and where $E = \{0, 2, 4, \dots\}$ is the set of even integers. Note that in computational implementations, we truncate this sum at some term, λ_{\max} . Whence, it follows that the matrix elements for this potential can be calculated numerically to be of the form

$$\begin{aligned} V_{i,j} = \langle \phi_i | \hat{V} | \phi_j \rangle = & -2 \sum_{\lambda \in E} \left(\int_0^\infty dr \varphi_{k_i, \ell_i}(r) \frac{r_{<}^\lambda}{r_{>}^{\lambda+1}} \varphi_{k_j, \ell_j}(r) \right) \left(\sqrt{\frac{4\pi}{2\lambda+1}} \langle Y_{\ell_i}^{m_i} | Y_\lambda^0(\Omega) | Y_{\ell_j}^{m_j} \rangle \right) \\ & \times \delta_{\pi_i, \pi_j} \delta_{m_i, m_j} \end{aligned} \quad (11)$$

where $\pi_i = (-1)^{\ell_i}$ is the parity quantum number.

Basis Symmetry

Due to the axial symmetry of the H_2^+ potential, and thus the Hamiltonian for the electron in this molecule, we may choose a symmetrised basis $\mathcal{B}^{(m, \pi)}$ with specified azimuthal angular momentum, m , and parity, π . Furthermore, due to the computational constraints, we restrict our basis to having $\{N_\ell\}_{\ell=0}^{\ell_{\max}}$ radial functions per ℓ , with exponential falloffs $\{\alpha_\ell\}_{\ell=0}^{\ell_{\max}}$. For simplicity, we select $N_\ell = N_0$, and $\alpha_\ell = \alpha_0$, for each $\ell = 0, \dots, \ell_{\max}$.

Radial Grid

We utilise a radial grid of the form

$$\{r_i = d_r \cdot (i - 1)\}_{i=1}^{n_r} \quad (12)$$

with n_r is the smallest integer such that

$$d_r \cdot (n_r - 1) \geq r_{\max}. \quad (13)$$

Note that when we numerically evaluate matrix elements of potentials which are singular as $r \rightarrow 0$, we handle these integrals by searching for the first r_i for which $V_i = V(r_i)$ is non-singular and evaluating the integral from this point forwards.

Computational Parameters

Across all computations performed, we have utilised $\alpha = 1$, $\lambda_{\max} = 10$, $d_r = 0.1$ and $r_{\max} = 75$. Hence, to denote a selection of computational parameters, we shall use the notation

$$\mathcal{B}_{N_0, \ell_{\max}}^{(m, \pi)} \quad (14)$$

to indicate that the calculation has been performed with the Laguerre basis, with m, π symmetries, with N_0 radial functions per ℓ , and with $\ell = 0, \dots, \ell_{\max}$.

Computational Procedure

The Hamiltonian for the H_2^+ molecule was diagonalised in the basis $\mathcal{B}_{N_0, \ell_{\max}}^{(m, \pi)}$, for $\pi \in \{-1, +1\}$, $m \in \{0\}$, $N_0 \in \{2^0, \dots, 2^5\}$, and $\ell_{\max} \in \{0, \dots, 6\}$, across a range of axial-distance values $R \in \{0.5, 1.0, \dots, 10.0\}$.

1.1 Comparison with Accurate Potential-Energy Curve for $1s\sigma_g$.

The convergence of the H_2^+ potential-energy curve (PEC), for the $1s\sigma_g$ state, is shown for increasing ℓ_{\max} in [Figure 1](#), and for increasing N_0 in [Figure 2](#). It can be seen by comparing the two figures that increasing N_0 past a certain point does little to improve the accuracy of the PEC ($N_0 = 2^4$ and $N_0 = 2^5$ yield essentially identical PECs), while on the other hand, increasing ℓ_{\max} continues to yield improved accuracy of the PEC (at least up to $\ell_{\max} = 6$).

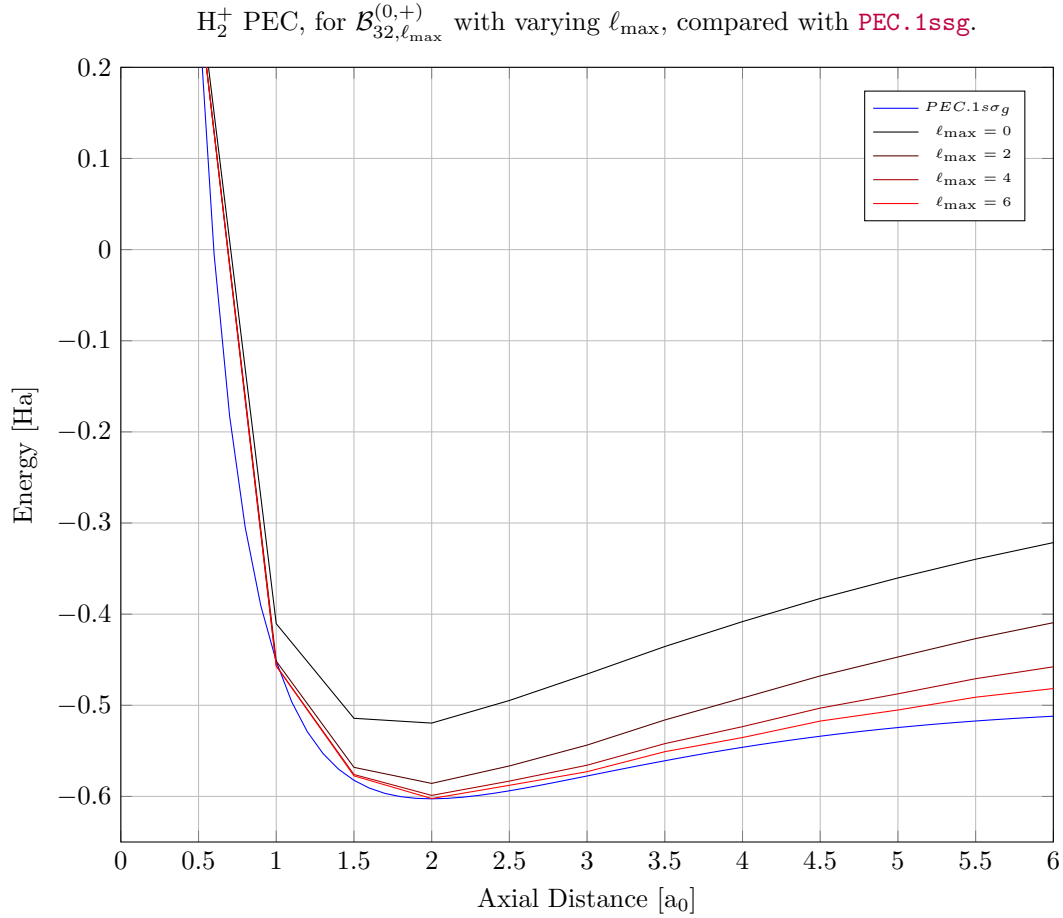


Figure 1: The potential energy curves, for $\ell_{\max} = 0, 2, 4, 6$, obtained by diagonalising the H_2^+ Hamiltonian in the bases $\mathcal{B}_{32,\ell_{\max}}^{(0,+)}$ (shown in black-to-red), are compared with the accurate potential energy curve provided in **PEC.1ssg** (shown in blue). It can be seen that calculated PECs do converge to the accurate PEC, with a non-negligible increase in accuracy with increasing ℓ_{\max} .

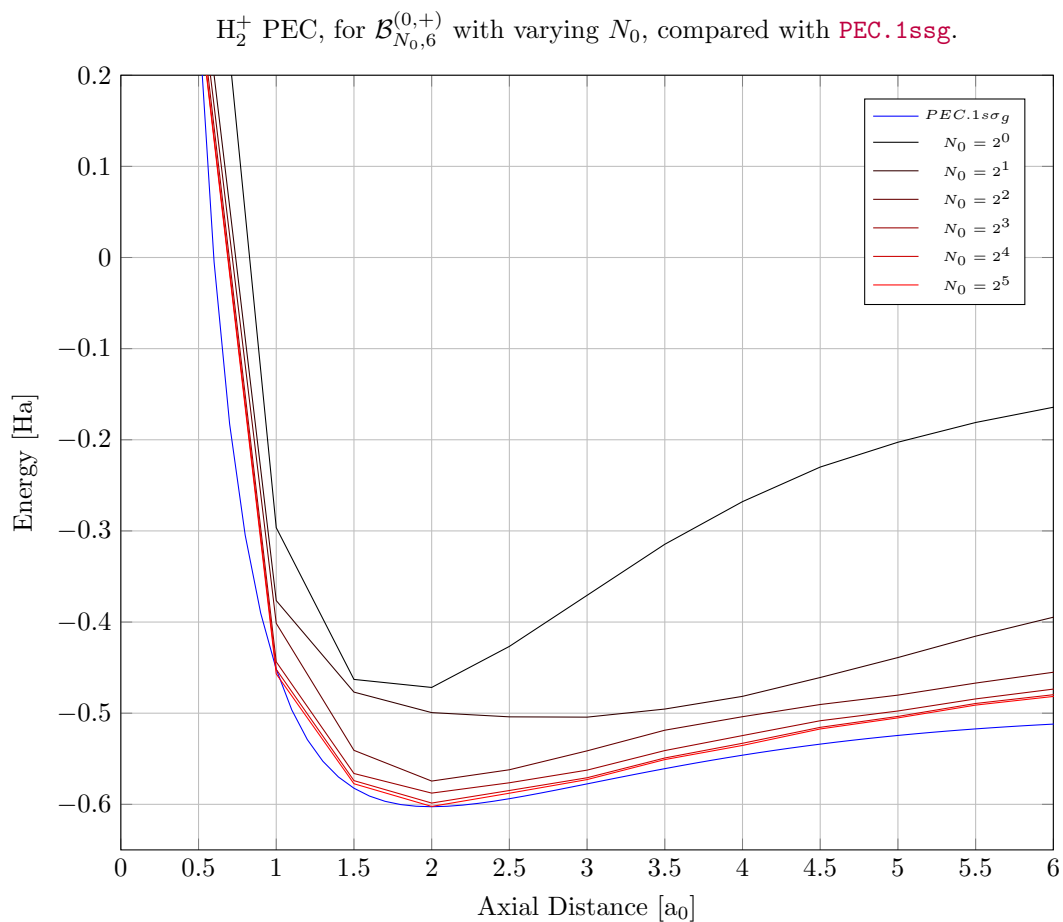


Figure 2: The potential energy curves, for $N_0 = 2^0, \dots, 2^5$, obtained by diagonalising the H_2^+ Hamiltonian in the bases $\mathcal{B}_{N_0,6}^{(0,+)}$ (shown in black-to-red), are compared with the accurate potential energy curve provided in **PEC.1ssg** (shown in blue). It can be seen that calculated PECs do converge to the accurate PEC, however the computational cost increases dramatically for diminishing improvements in the accuracy of the PEC.

1.2 Comparison with Accurate Potential-Energy Curve for $2p\sigma_u$.

The convergence of the H_2^+ potential-energy curve (PEC), for the $2p\sigma_u$ state, is shown for increasing ℓ_{\max} in Figure 3, and for increasing N_0 in Figure 4. It can be seen by comparing the two figures that increasing N_0 past a certain point does little to improve the accuracy of the PEC ($N_0 = 2^4$ and $N_0 = 2^5$ yield essentially identical PECs), while on the other hand, increasing ℓ_{\max} continues to yield improved accuracy of the PEC (at least up to $\ell_{\max} = 5$).

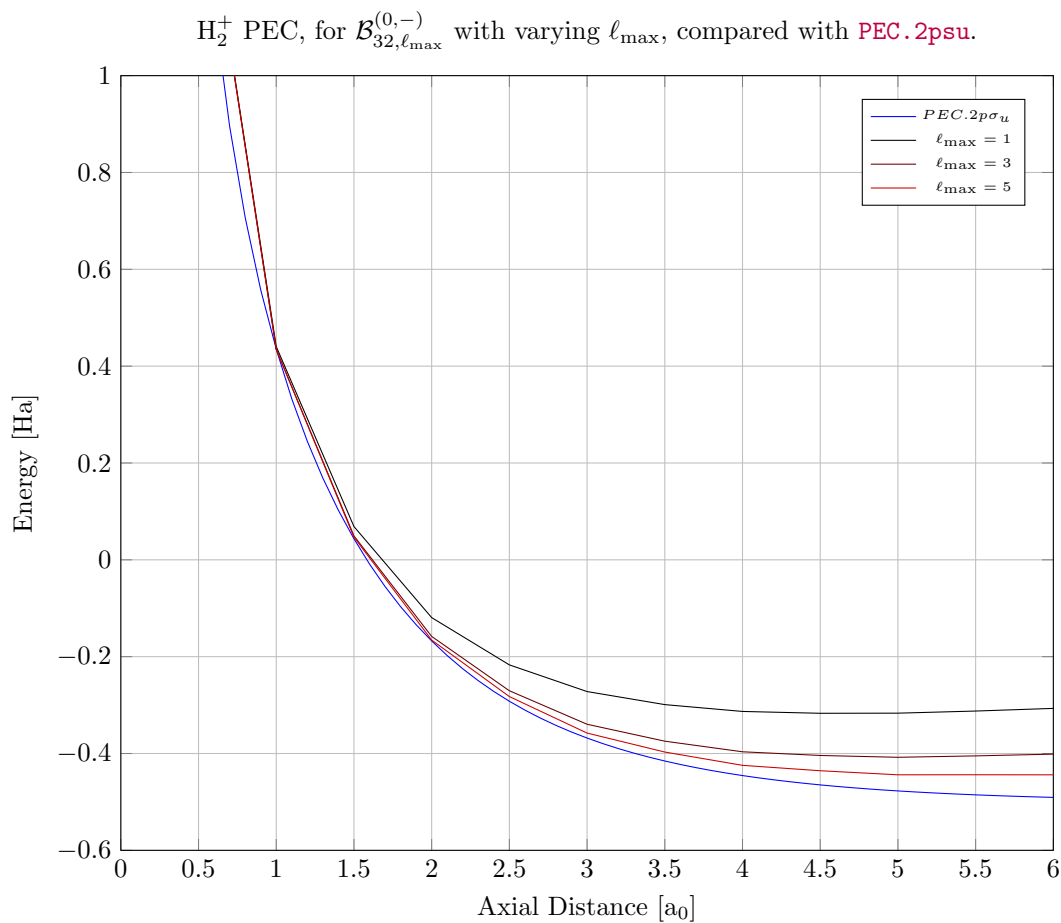


Figure 3: The potential energy curves, for $\ell_{\max} = 1, 3, 5$, obtained by diagonalising the H_2^+ Hamiltonian in the bases $\mathcal{B}_{32,\ell_{\max}}^{(0,-)}$ (shown in black-to-red), are compared with the accurate potential energy curve provided in **PEC.2psu** (shown in blue). It can be seen that calculated PECs do converge to the accurate PEC, with a non-negligible increase in accuracy with increasing ℓ_{\max} .

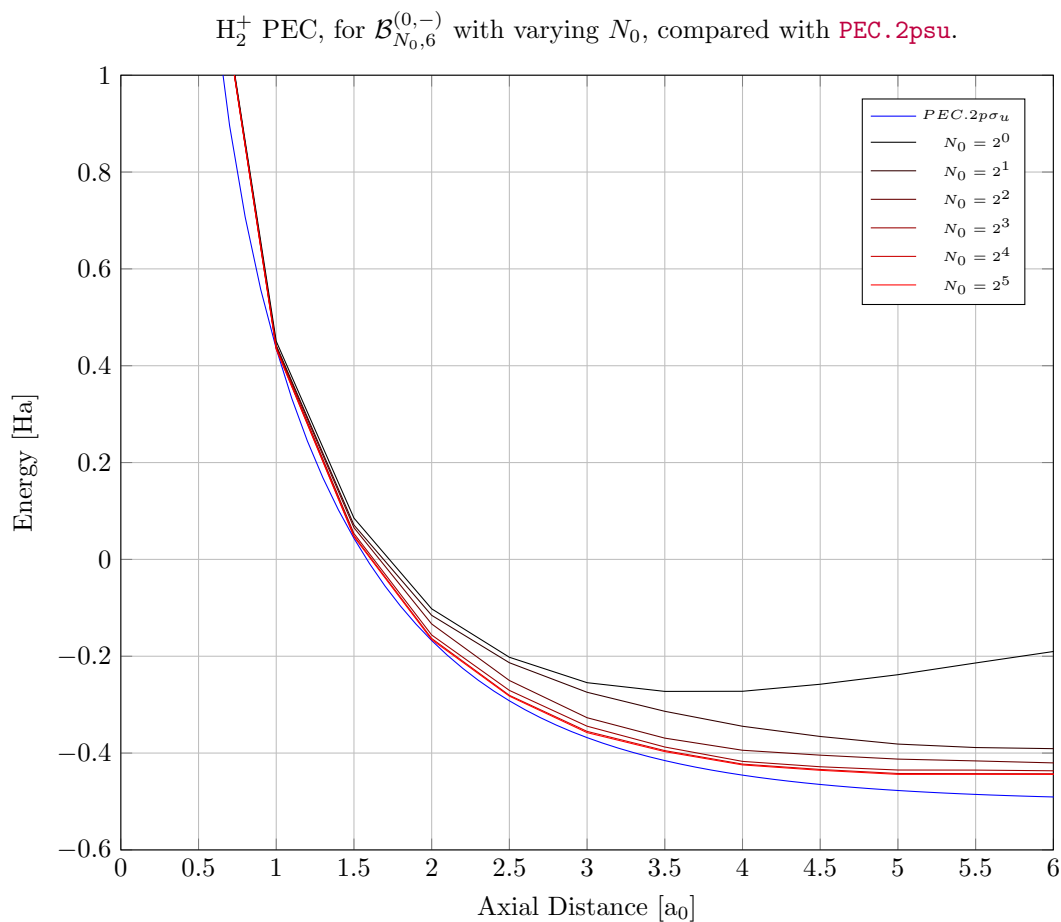


Figure 4: The potential energy curves, for $N_0 = 2^0, \dots, 2^5$, obtained by diagonalising the H_2^+ Hamiltonian in the bases $\mathcal{B}_{N_0,6}^{(0,-)}$ (shown in black-to-red), are compared with the accurate potential energy curve provided in **PEC.2psu** (shown in blue). It can be seen that calculated PECs do converge to the accurate PEC, however the computational cost increases dramatically for diminishing improvements in the accuracy of the PEC.

2 H_2^+ Vibrational Wave Functions

Details of Relevant Theory and Code

2.1 Vibrational Wave Functions for $1s\sigma_g$ PEC.

The vibrational wave-functions of H_2^+ , in the $1s\sigma_g$ state, were calculated by diagonalising vibrational Hamiltonian in a Laguerre basis, $\mathcal{B}_{128,0}^{(0,+)}$, with the vibrational potential matrix elements being calculated numerically, after interpolating **PEC.1ssg** onto the radial grid. The first 10 vibrational wavefunctions are shown in **Figure 5**; note that the wavefunctions have been shifted by their corresponding vibrational energies, and scaled arbitrarily to make their presentation more convenient.

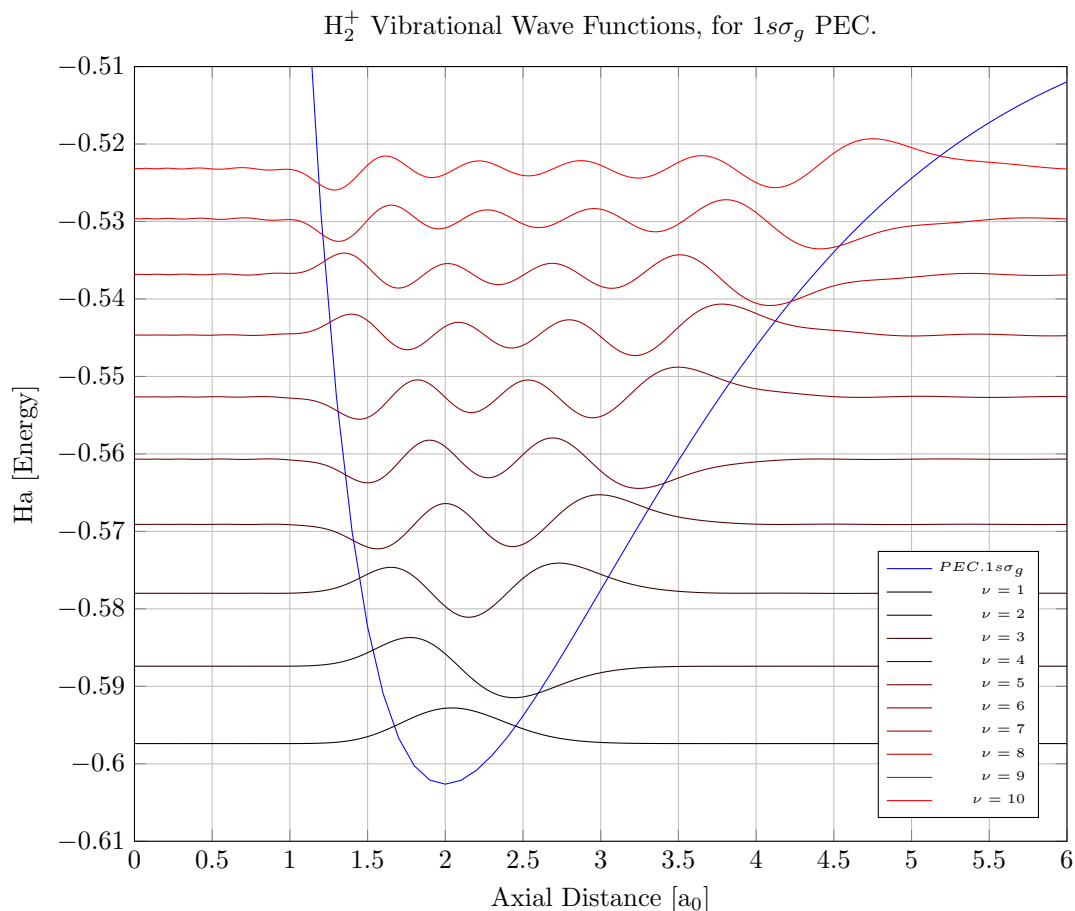


Figure 5: The first 10 vibrational wavefunctions, $\psi_\nu(r)$, are shown in the form $a\psi_\nu(r) - \epsilon_\nu$, where $a = 0.0035$, and ϵ_ν is its corresponding vibrational energy. These wavefunctions were calculated by diagonalising the H_2^+ vibrational Hamiltonian in a Laguerre basis $\mathcal{B}_{128,0}^{(0,+)}$, using the accurate $1s\sigma_g$ PEC (shown in blue).

2.2 Lowest-Energy, $\nu = 0$, Vibrational Wave Functions for $1s\sigma_g$ PEC, for each Isotopologue of H_2^+ .

The ground-state vibrational wavefunctions are shown for H_2^+ and its isotopologues (indexed by their reduced mass, μ) for the $1s\sigma_g$ state in Figure 6. Note that the wavefunctions have been shifted by their vibrational energy, and scaled arbitrarily to allow for easier visual comparison. It can be seen that the vibrational ground-state energy decreases as the reduced mass of the isotopologue increases. However, the overall behaviour is very similar, being a uni-modal wavefunction confined to the deepest region of the PEC. As the reduced mass increases, the wavefunctions become increasingly confined to this region.

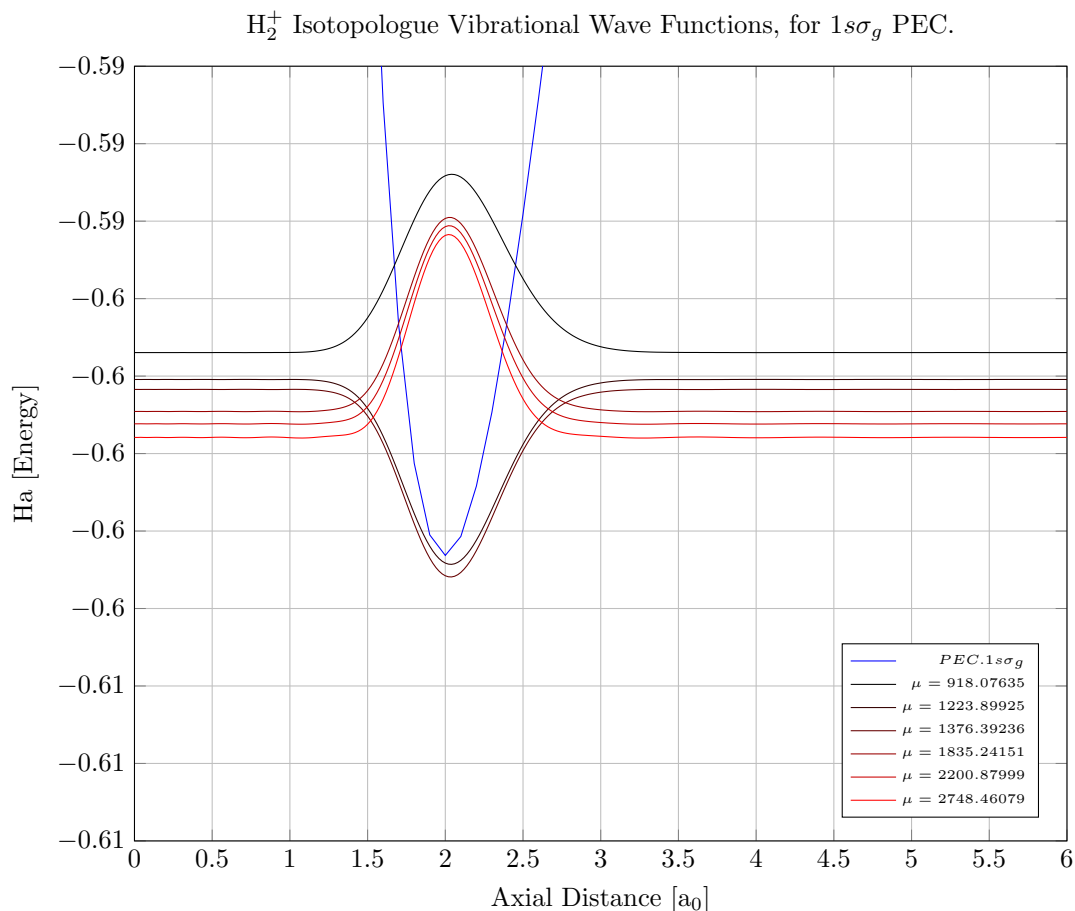


Figure 6: The ground state, $\nu = 0$, vibrational wavefunctions for H_2^+ and its isotopologues, are shown in the form $a\psi_0^{(\mu)}(r) - \epsilon_\nu^{(\mu)}$, where $a = 0.0035$, and $\epsilon_\nu^{(\mu)}$ is the vibrational energy corresponding to the isotopologues ground state. These wavefunctions were calculated by diagonalising the H_2^+ vibrational Hamiltonian in a Laguerre basis $\mathcal{B}_{128,0}^{(0,+)}$, using the accurate $1s\sigma_g$ PEC (shown in blue). Note that the phase-shift inversion of the first two isotopologues is a by-product of the diagonalisation procedure and has no physical significance.